An Integrated Flow–Electric–Thermal Model for a Cylindrical Li-Ion Battery Module with a Direct Liquid Cooling Strategy

(article starts on next page)

An Integrated Flow–Electric–Thermal Model for a Cylindrical Li-Ion Battery Module with a Direct Liquid Cooling Strategy

Litao Yin, Zeyang Geng, Are Björneklett, Elisabeth Söderlund, Torbjörn Thiringer, and Daniel Brandell*

An integrated model is constructed for a Li-ion battery module composed of cylindrical cells by coupling individual first-order equivalent circuit models (ECMs) with a 3D heat transfer model, also considering the fluid flow dynamics of the applied cooling liquid, and bench-marked against experimental data. This model simulates a representative unit of the battery module with direct liquid cooling in a parallel configuration. Instead of assigning specific values to the featured parameters involved in the ECMs, they are here defined as 4D arrays. This makes it possible to simultaneously consider the effect of the state of charge, current rate, and temperature on the battery dynamics, making the model more adaptive, versatile, and connectable to the battery cell electrochemistry. According to the simulation results, the model employing state-dependent battery properties fits better with the experimental cooling results. Additionally, the temperature uniformity of the module with a parallel cooling configuration is improved compared to a serial configuration. However, the increase of the absolute core temperature cannot be directly controlled by the surface cooling due to the slow heat transport rate across the battery material. The simulations also provide directions for the modification of module design, to the potential benefit of battery pack developers.

L. Yin, D. Brandell
Department of Chemistry - Ångström Laboratory
Uppsala University
751 21 Uppsala, Sweden
E-mail: daniel.brandell@kemi.uu.se

Z. Geng, T. Thiringer
Department of Electrical Engineering
Division of Electric Power Engineering
Chalmers University of Technology
412 96 Göteborg, Sweden

A. Björneklett, E. Söderlund
APR Technologies AB
745 39 Enköping, Sweden

The ORCID identification number(s) for the author(s) of this article can be found under https://doi.org/10.1002/ente.202101131.

1. Introduction

Lithium-ion batteries (LiBs) are on their way to becoming a dominating energy storage technology, especially for application in electric vehicles,[1,2] due to their excellent performance in terms of combinations of energy density, power capability, energy efficiency, and cycle life. In recent decades, there have been plenty of investigations, both using experimental measurements[3–5] and simulations,[6–9] aiming to improve the safety, energy, and power of LiBs. This has led to a consensus that the performance of LiBs is largely dependent on their operational temperature,[10–14] explaining the growing interest in thermal control of LiBs, both at the cell and system level and to increased efforts in coupled thermal and electrochemical modeling of cell behavior.[15–19]

However, most of the existing coupled thermal and electrochemical models are either built on the single-cell level, which is not applicable in the investigation of the effect of the battery module design. Alternatively, they are built based on the most simply operational air-cooling system. The aim of the present study is, therefore, to establish an integrated model at the battery module level, which can take into account the simultaneous and interdependent thermal behavior of different cells and the effects from relevant multi-physical fields caused by different cooling strategies, incorporating fluid flow and heat transfer across both fluid and solid domains.

Since the thermal behavior of the batteries/module is determined by the balance between heat generation and dispassion rate, the first step to building a convincing integrated model is to understand the heat generation within the battery, i.e., to build a precise thermal model. The existing thermal models for LiBs can be classified into lumped-parameter models,[20] electric–thermal models,[6,21] electrochemical–thermal models,[22,23] and thermal runaway models.[24,25] Among these, the electrochemical–thermal model can provide the most detailed information on the battery physics, which makes it possible to extract heat generated from different components,[26] making it favorable from a battery design point of view. For example, Kim et al. discussed the impact of geometry and position of the tabs on the temperature gradient in an operated battery,[27] while Lee et al.[28] found that the heat

**ADVANCED
SCIENCE NEWS**
www.advancedsciencenews.com

Energy Technology
Generation, Conversion, Storage, Distribution
www.entechnol.de

generated from tabs was the main reason for the non-uniform temperature distribution in a battery.

However, the disadvantage of such a comprehensive model is the associated large computational load.[29] Especially for a large-format battery module, which may include hundreds or even thousands of cells, the complexity and computational cost of employing an electrochemical-thermal model will be impractically large, let alone combined with a 3D flow dynamic model. Thus, a lumped-parameter model or an equivalent circuit model (ECM) is more often used in the simulation of large-format battery modules.[30,31] In such models, the heats generated from a single cell are generally calculated either by using the empirical energy balance, as originally proposed by D. Bernardi et al.,[32] or by using Ohm's law assuming the internal resistance as a fixed value or as a 1D variation (usually as a function of the state of charge, SOC).[33,34] However, considering that the battery behavior is also largely dependent on temperature and C-rate, the relevant battery physics may be oversimplified through the abovementioned approach. While a few approaches have been employed to account for such effects,[35–37] a complete multi-factor-impact, including the joint effects from temperature, SOC, and C-rate, has not been considered in the existing thermal models so far. Therefore, a new equivalent circuit model (ECM) is proposed herein, using several 4D arrays that define the relevant featured parameters.

In real applications, such as EV batteries, an unexpected temperature increase of the battery module is generally handled through appropriate module design, and advanced cooling strategies, e.g., active cooling with air or liquid, or passive cooling with phase change materials—are usually employed. Among these, the air-based cooling strategy is frequently used by EV manufacturers due to its simplicity and low cost.[38–40] However, the efficiency of air-based cooling is often insufficient for large format battery modules, especially when operating at a relatively high C-rate.[41] In contrast, liquid-based cooling is considerably more efficient due to the relatively high thermal capacity and thermal conductivity of the liquid coolant. Specifically, there exist two different liquid-based cooling strategies: indirect liquid cooling and direct liquid cooling.[42] For indirect liquid cooling, the complex module design and the potential leakage of the coolant are the most challenging problems for practical applications. Currently, EV manufacturers such as Tesla and GM are adopting indirect liquid cooling strategies for their battery modules.[43–45] Direct liquid cooling, in turn, has not been as widely used in the mass-produced EV market, but is primarily used conceptually in high-performance EVs and EV racing.[46,47] This may partly be due to the high cost of the dielectric liquids, which are required by the direct (immersion) cooling technology, and partly due to the lack of awareness of the capability of this cooling technology. In fact, increasing research efforts have shown that direct liquid cooling is a highly promising cooling strategy for the large format battery module used in EVs,[48] and may advance in the next generation of battery thermal management systems. Thus, in this study, we will apply the established integrated model to investigate the thermal behavior of a large battery module that employs a direct liquid cooling strategy, thereby providing directions for the battery thermal management system design. Since the parallel configuration (as compared to a serial configuration) of the battery arrangement

in the large module is more favorable for temperature uniformity,[6,48] it is the focus of the current study.

2. Model Development

2.1. Module Structure and Representative Unit for Modeling

Figure 1a shows the schematic of the battery module with the employment of a direct liquid cooling strategy and with a parallel cooling configuration. Multiple battery modules are connected to a common rail inlet and outlet that are part of the heating, ventilation, and air conditioning (HVAC) system of the vehicle. Figure 1b shows the battery arrangement in the module with engraved liquid flow channels. The top cover (not shown) has a similar structure. To obtain a more homogeneous flow rate across the module, the depth of the channels is larger on the inlet side than on the outlet side. Simulations show that a linear grading of the channel depths results in a not perfect, but much more uniformly distributed flow rate compared to a design with identical channel depths. In addition, to achieve a relatively high energy and power density, the battery module is designed using a staggered arrangement. This means that the closest distance between each of the two neighboring cells is constant, and is set to be 0.5 mm. The enlarged illustration in Figure 1b shows that a cylindrical isolator rod is inserted into each of the coolant units and is tangentially contacted with all three surrounding cells. This helps to warrant that all cells are separated effectively and uniformly.

The cooling liquid polyalphaolefin (PAO) flows through the module in the vertical/axial direction, as shown by the arrows in Figure 1a. Even though the module is designed to include a large number of cells for usage in (for example) an electric vehicle, owing to the advantage of the parallel cooling configuration, the cooling condition for each cell in the module should be repeatable. To make the computations practically solvable, a representative unit of the cooling liquid and its neighboring batteries is therefore abstracted and simulated. As shown in Figure 1c, the actual simulation domain contains three 1/6 cells, the isolator rod, and the cooling liquid flowing through the center of it. The upper and bottom parts correspond to the graded channels, which together collect and distribute the cooling liquid uniformly through the module. The relevant geometric factors used in the model are given in **Table 1**.

2.2. Overview of the Integrated Flow–Electric–Thermal Model

In this study, a commercial @FEM-based software, COMSOL Multiphysics, was used to build the model and conduct the numerical simulations. The software can integrate several different physical fields by a two-direction (full) coupling, which makes it possible to capture the transient development of the whole simulation system. Herein, the battery will generate heat under usage, and this heat will be transported across the battery materials and further transported to the cooling liquid, and finally dissipate out of the battery module. Both the heat generation rate and the flow dynamics of the cooling liquid will affect the final cooling efficiency. Thus, as illustrated in **Figure 2**, it is necessary to take all abovementioned kinetic processes into account in the model.

Specifically, due to that, the flow rate of the cooling liquid is not high enough to cause turbulence, a laminar flow interface
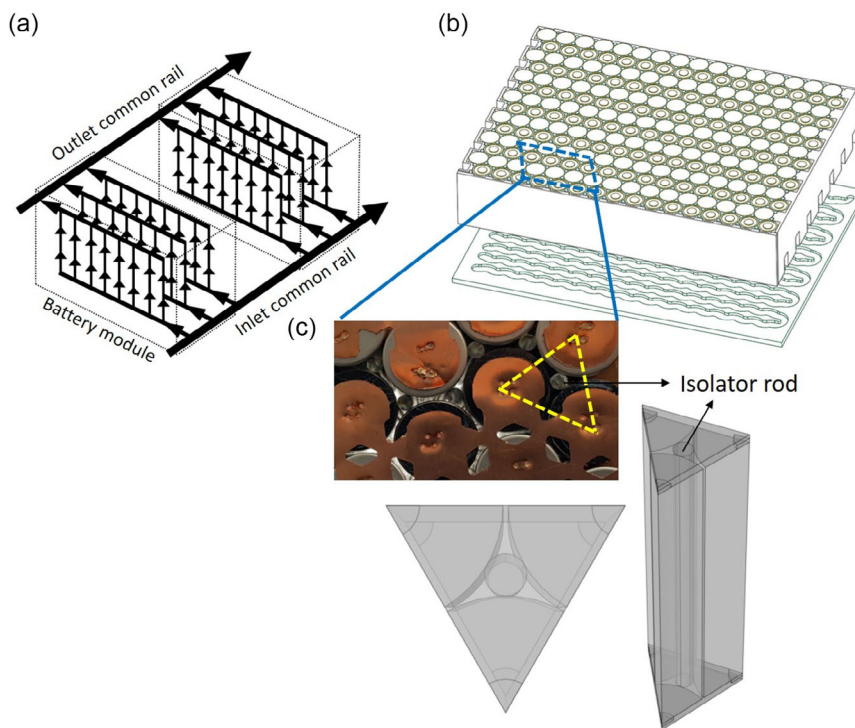
ADVANCED
SCIENCE NEWS
www.advancedsciencenews.com

Energy Technology
Generation, Conversion, Storage, Distribution
www.entechnol.de

Figure 1. a) Configuration of the cooling liquid flow pattern showing the inlet and outlet common rail that connect different battery modules; b) Battery arrangement in the module and the enclosure bottom (top cover has similar structure) with engraved liquid flow channels where the enlargement shows that a cylindric isolator rod is inserted into each of the coolant unit and tangentially contacted with all three surrounding cells; c) Schematic of the representative unit simulated in the model which includes three 1/6 cell, one isolator rod and the cooling liquid flowing in between.

is used in the integrated model to describe the flow dynamic and calculate the stationary flow rate surrounding each cell. This flow rate will be used as one of the boundary conditions in the heat transfer interface. Three electrical circuit models (ECMs) are used to simulate corresponding battery properties and calculate the heat generation rate during operation. These will be integrated into the heat transfer interface as the kinetic heat source. The main parameter calculated from the heat transfer interface is the temperature. By averaging the battery material domains for each cell, the dynamically changing temperature is fed back to the ECMs, and used to estimate the predefined SOC/C-rate/temperature-dependent battery properties. Based on these new properties, the heat generated from the batteries is updated once at each time step throughout the simulation. Since the viscosity of typical dielectric liquids

decreases with increasing temperature[49,50] and an increasing flow rate due to lower viscosity leads to more effective cooling, this should provide a temperature stabilizing effect. The model here, however, assumes that such temperature effects on the flow dynamics are relatively small, and the updated temperature is, therefore, not used as input to the laminar flow interface. Instead, the flow dynamic/rate is computed at the beginning of the simulation. Thereby, the integrated model will converge more easily and save computational resources. It should be noted that a more advanced flow dynamic model can be envisioned in future work which takes the complexity of nonideal flow into account.

Table 1. Geometric parameters used in the model.

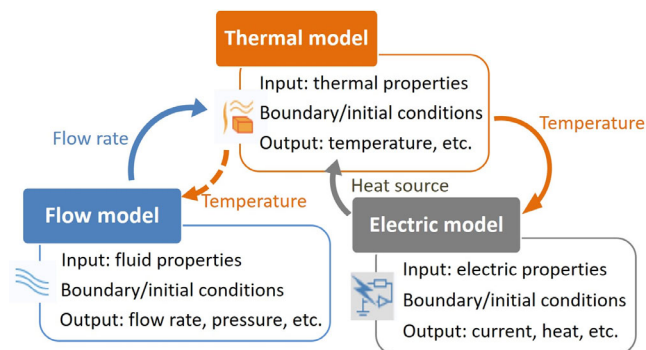| Geometric parameters	Value
Battery diameter, d_batt [mm]	21
Battery height, h_batt [mm]	70
Terminal radius, r_term [mm]	3
Terminal height, h_term [mm]	1
Space between different batteries, d_spa [mm]	0.5
Height of the liquid collection space, h_liq [mm]	3

Figure 2. Schematic of the integrated electric-heat transfer-fluid flow model.

2.3. Governing Equations and Boundary Conditions

2.3.1. Laminar Flow Interface

As mentioned earlier, it is assumed that the flow dynamics of the cooling liquid surrounding each of the batteries can be described by a laminar flow, since the investigated flow rate is relatively slow (the Reynolds numbers calculated with the simulated battery module design and for all the flow rates investigated are less than 50). Relevant flow dynamics can be calculated based on the continuity equation and momentum conservation equation as follows, in which ρ is the density, p is the static pressure, μ is the dynamic viscosity, $\mathbf{u}$ and $\mathbf{I}$ are the flow rate vector and unit vector, respectively.

$$\rho \nabla \cdot \mathbf{u} = 0 \tag{1}$$

$$\rho (\mathbf{u} \cdot \nabla) \mathbf{u} = \nabla \cdot [-p\mathbf{I} + (\mu(\nabla \mathbf{u} + (\nabla \mathbf{u})^T)] \tag{2}$$

Figure 1 shows that the liquid phase includes the upper and bottom parts, corresponding to both the liquid distributor and the liquid in the center of three neighboring battery cells. The liquid flows through the module from the top surface (inlet) to the bottom surface (outlet) vertically. With respect to the boundary conditions, a normal inflow velocity of $0.001\,\mathrm{m\,s^{-1}}$ is defined at the top surface, and a free outlet condition is defined at the bottom surface. The inflow velocity is calculated based on the real battery module design, in which a liquid pump is used to tune the flow velocity. The interface between the batteries and the liquid is defined as a wall, and the other vertical cross-sections are defined to be symmetric (insulation).

2.3.2. ECM

A first-order electrical circuit model, as shown in **Figure 3**, which includes one open-circuit voltage (V_{oc}), one resistor ($R0$), and one resistor–capacitor pair ($R1$–$C1$), is used to describe the electrochemical properties of the batteries in the integrated model. The terminal voltage (V_T) of such a battery model can be described as

$$V_T = V_{oc} - IR_0 - V_{RC} \tag{3}$$

where the second term on the right is the voltage drop caused by ohmic resistance and V_{RC} is the potential drop caused by the R–C pair. The transient voltage dynamics can then be calculated by
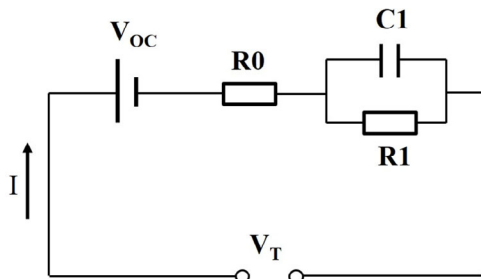
$$\frac{dV_{RC}}{dt} = -\frac{1}{R1 \cdot C1} \times V_{RC} + \frac{1}{C1} \times I \tag{4}$$

where $R1$ and $C1$ are the resistance and capacitance of the R–C pair. A very important advantage of the model proposed here is that all parameters involved in the ECM are updated based on SOC, C-rate, and temperature, instead of being fixed at a certain value for different operation conditions. Without this feature, the usefulness of the model would be very limited. Detailed experimental setup and data fitting are introduced in Section 2.4.

2.3.3. Heat Transfer Interface

Heat transfer in both solid and liquid phases is used to calculate the temperature distribution in the battery module and follows the relation

$$\rho C_p \frac{\partial T}{\partial t} + \rho C_p \mathbf{u} \cdot \nabla T + \nabla \cdot (-k_T \nabla T) = Q \tag{5}$$

where ρ, C_p, k_T are the density, thermal capacity, and thermal conductivity of the material in the corresponding domain, e.g., the cooling liquid or the solid battery material. In this context, the battery material is assumed to be a uniform domain with anisotropic thermal conductivity, which can be calculated by lumping properties of different layers in parallel ($k_{T,ang} = \frac{\sum L_i k_{T,i}}{\sum L_i}$) or in series ($k_{T,r} = \frac{\sum L_i}{\sum L_i/k_{T,i}}$),[19,51] with $k_{T,ang}$, $k_{T,r}$ representing the thermal conductivity of the battery material in the tangential and radial directions and L_i, $k_{T,i}$ denoting the thickness and thermal conductivity of different layers of the cell, respectively. $\mathbf{u}$ is the flow rate calculated from the laminar flow interface, while Q is the heat source calculated from the electrical circuit models, and can be calculated according to[32]

$$Q = I[(V_{OC} - V_T) - T\frac{\partial V_{OC}}{\partial T}] \tag{6}$$

It should be noted that the featured parameters used in the abovementioned ECM, e.g., $R0$, $R1$, and $C1$, are dependent on the operation conditions, including SOC, C-rate, and temperature. With respect to the boundary conditions, at the top surface (inlet), a fixed temperature is defined, which is considered determined by the external battery thermal management system (BTMS). A free outflow condition is then defined at the bottom surface.

2.4. Parameterization of ECM

It is commonly acknowledged that the properties of LiBs are dependent largely on the operational conditions, for instance, the SOC range in usage, charge/discharge rate, and temperature—and then not only the temperature of the surrounding environment, but also the internal temperature developed within the battery cells. To get more precise simulation results, the parameters used in the ECMs here are defined as a series of 4D arrays obtained by interpreting separated data sets that are measured under different conditions, instead of fixed to certain values.[42]

Figure 3. Schematic of the first order electrical circuit model used in the integrated model.

2.4.1. Experimental Setup

Parameterization of the first-order electrical circuit model, as shown in Figure 3, includes identification of the open-circuit voltage (V_{oc}), ohmic resistance ($R0$), resistance ($R1$), and capacitance ($C1$) of the R–C pair. Among these, V_{oc} was determined by cycling the battery with a low charge/discharge rate (using the average value), and the others were determined based on a series of pulse-relaxation tests.[20] Specifically, both the measurements and simulations in this study were conducted on a 4.8 Ah commercial 21 700 cylindrical cell. As shown in **Figure 4**a, the tested batteries were put in a thermal chamber and the ambient temperature was controlled. To warrant reproducibility, two parallel tests were conducted at the same time (the two parallel batteries were put far away enough to avoid disturbances). The test equipment is an advanced battery tester PEC ACT0550 and a temperature sensor PT100 is used to monitor the surface temperature of the battery. Here, three temperatures 5, 20, and 35 °C were chosen for the measurements, allowing for the temperature dependency of the battery properties to be determined. All tests were also conducted with different C rates (1C, 2C, 3C), meaning that there were nine different combinations of temperature and C-rate which could be used for the interpolation.

Before the real tests, the new batteries were cycled with a 1C CC-CV protocol five times to initialize the battery. The high and low voltage limits were 4.2 and 2.5 V, respectively, and the cutoff current for the CV test was C/20 (0.24 A). After this, the V_{oc} for both charge and discharge was measured using a C/20 CC-CV protocol, with the cutoff current for the CV test set to C/100 (48 mA). The results are shown in Figure 4b with a high reproducibility of the results from the two cells. Between charge and discharge, a rest of 30 min was inserted to let the system reach thermal balance.

The other parameters $R0$, $R1$, and $C1$ were determined based on pulse-relaxation tests.[20] These were conducted during discharge, considering that the EV battery charge process is normally conducted under controlled conditions. Since the discharge is dependent on the load (or road) conditions, it is more challenging and valuable to investigate from a thermal management point of view. Specifically, the battery was first charged to 4.2 V with a C/2 CC-CV protocol, and the cutoff current was C/50 for the CV process. The battery was then relaxed for 2 h to reach the thermal equilibrium state. Afterward, the battery was first discharged to 90% SOC using different C rates. For instance, this process lasted for 6, 3 or 2 min for 1, 2, and 3C discharge, respectively. Then, the current was cut and the battery was relaxed for 1 h. The voltage evolution during this relaxation was recorded to calculate the relevant parameters ($R0$, $R1$, $C1$) at this SOC level. The abovementioned discharge procedures were then repeated in 10% SOC intervals until the low voltage limit (2.5 V) was reached. The discharge current and recorded voltage, taking 1C current as an example, are shown in Figure 4c.
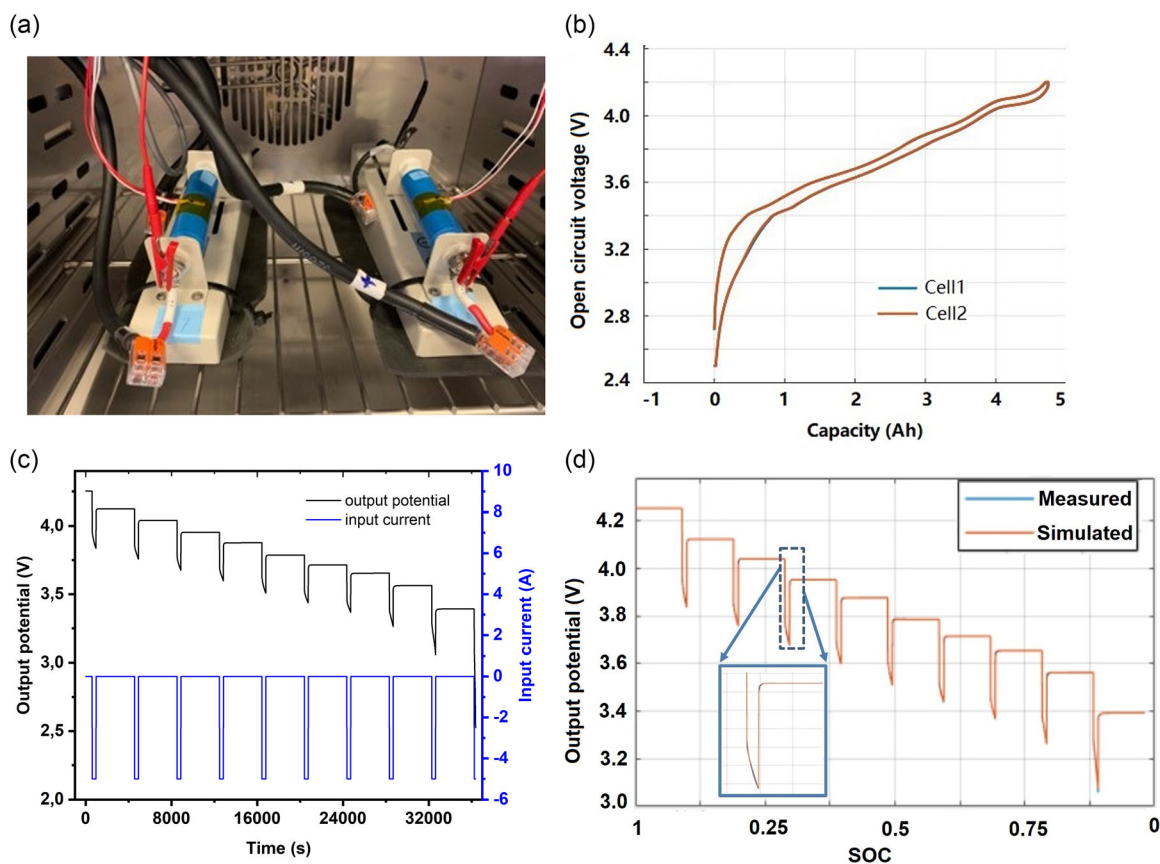

Figure 4. a) Experimental setup for pulse-relaxation test; b) Open-circuit voltage (V_{oc}) measured for both charge and discharge processes; c) 1C discharge current and recorded voltage for the pulse-relaxation test; d) Fitting result of the voltage by using the Parameter Estimator of Simulink.

Considering that the battery is placed inside the thermal chamber, and the battery temperature is not supposed to increase largely during the short discharge period for each of 10% SOC, and also taking the relaxation period into account, the battery temperature can be controlled effectively at the set points, and the measured data can be used to reflect the operando battery properties at certain temperatures.

2.4.2. Parameter Dependence on SOC, C-rate and Temperature

Based on the recorded voltage evolution, the parameters involved in the ECM can be determined under different conditions. Among these, the ohmic resistance ($R0$) can be calculated according to Ohm's law

$$R0 = \frac{\Delta V_{t=0}}{I} \tag{7}$$

$\Delta V_{t=0}$ is the abrupt voltage change when the current is switched off, while I is the applied pulsed current. The temporal evolution of the relaxation voltage can be derived by solving Equation (4) and can be written as

$$V_{RC}(t_{relax}) = IR1\left(1 - e^{-\frac{t_{pulse}}{R1C1}}\right)\left(1 - e^{-\frac{t_{relax}}{R1C1}}\right) \tag{8}$$

where t_{pulse} is the pulse duration. Till now, all parameters can be determined by fitting the experimentally measured voltage evolution to the simulated result based on the ECM shown in Figure 3. This can be done straightforwardly by, for example, using the parameter estimator in the APPS of Simulink.[52] Figure 4d shows one of the fitting results. Even though there are some (very) minor details that cannot be fitted precisely, the accuracy of the fitting result is acceptable considering the many assumptions used in the entire integrated model.

As mentioned, the parameterization is done for different combinations of operation conditions, including different SOC, C-rate, and temperature. **Figure 5**a–c shows an example of fitting results for R0, in which the nine lines correspond to the nine different combinations of C-rate (1C, 2C, 3C) and temperature (5, 20, 35 °C). SOC is drawn on the x-axis, and the parameter value ($R0$) is displayed on the y-axis. At low temperature (5 °C), it can be seen that $R0$ is relatively higher. This is expected, considering that mass transport in the electrolyte is inhibited, and thus the electrolyte conductivity is lower. Moreover, it can be seen for all temperatures that $R0$ decreases with increasing
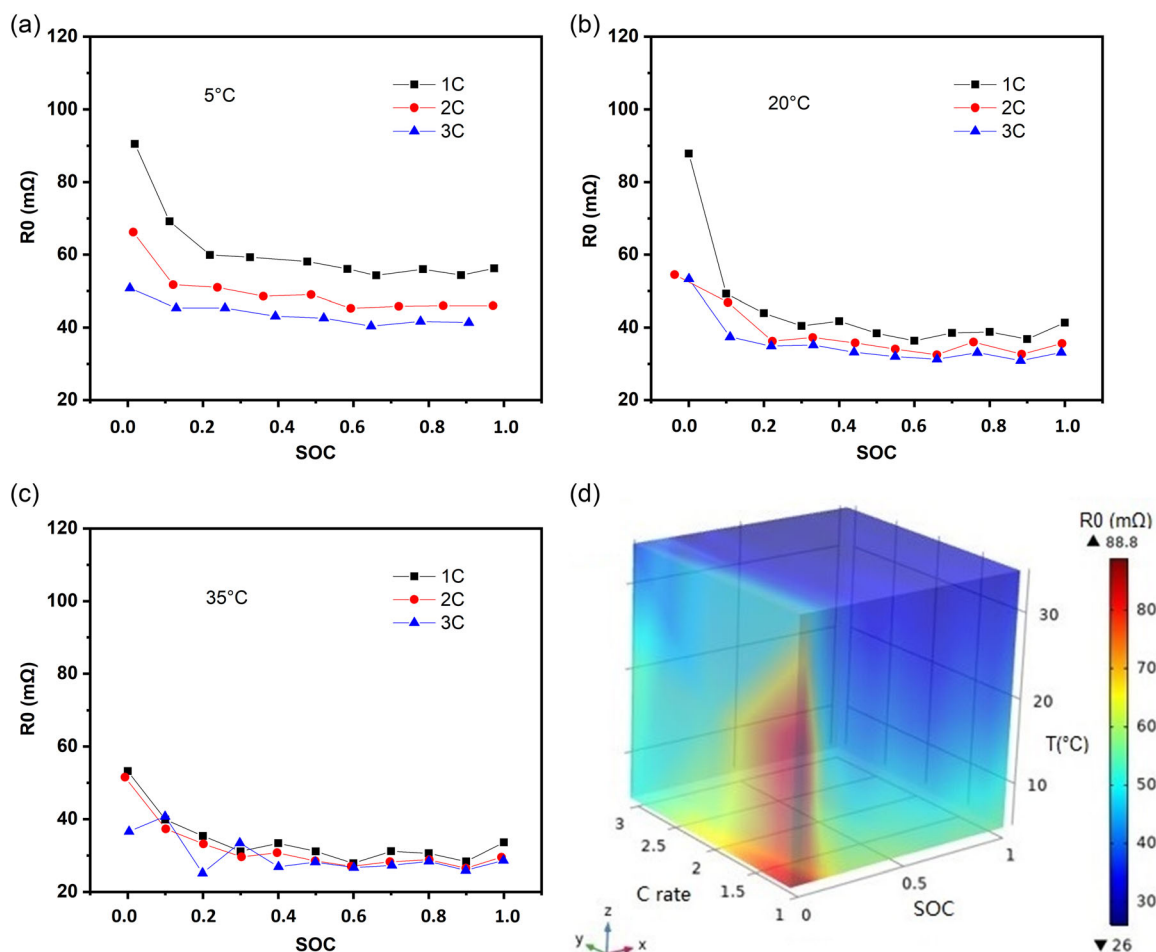

Figure 5. a–c) R0 estimated at different temperatures and C-rates a function of state of charge (SOC); d) Interpolated SOC/C-rate/temperature dependence of R0.

C-rate, but this trend is pronounced at a lower temperature. This can be explained by the fact that the temperature of the battery increased more at a higher discharge rate, and especially at lower ambient temperature. To take both the effect of temperature and C-rate into account, an interpolation based on all the displayed nine lines in Figure 5a–c was conducted, and the 4D array obtained is shown in Figure 5d. In this diagram, the x-, y-, z-axes display the SOC, C-rate, and temperature, respectively, and the color bar shows the $R0$ value. The same operations have been performed on the other parameters (for $R1$ and $C1$, see Figure S1 and S2 in the Supporting information), and all the obtained SOC/C-rate/temperature-dependent parameters were then used as input for the electrical circuit model, which in turn is part of the integrated model.

3. Model Validation

3.1. Experimental Setting

To validate the model established earlier, the same operating procedures were conducted in both experiments and simulations. Specifically, the measurements were done based on a module including 288 commercial 21 700 cylindrical cells, which are the same as those used in the model parameterization. To obtain a sufficiently large temperature difference between the battery cells and the coolant, thereby generating heat transfer characteristics that can be determined with reasonable accuracy, a relatively high discharge rate of 2C was applied when discharging the module from 90% SOC to 20% SOC. Under real-life driving conditions, a dynamic current pattern would naturally be more common. Nevertheless, the applied 2C constant discharge current covers the root mean square of the battery current during driving and thus allows for a margin regarding the real heat generation conditions. In addition, the direct liquid cooling with a parallel cooling configuration was used to control the battery temperature, i.e., the coolant flows in the vertical direction. Here, the coolant used was PAO and its relevant thermal properties are listed in **Table 2**. Even though there are limited examples of using PAO as immersion cooling fluid for batteries, it should be a highly promising option in the near future, especially for EVs. Compared with alternatives, PAO has several favorable features: low toxicity, wide working temperature range, and causing a more stable structure compared with mineral oil. In contrast to fluorinated coolants, it will not release additional fluorine during cell combustion.[53]

The flow rate of the coolant at the inlet of the battery module was set to 6 L min^{-1}, which is accomplished by a pump power of 5–10 W. This is equivalent to the boundary condition defined on the upper interface of the simulated unit with an inflow velocity of 0.001 m s^{-1}. It should be noted that the initial temperature of the coolant is controlled to 12 °C here, to avoid battery overheating when used at a relatively high C-rate. Eight temperature sensors, negative temperature coefficient (NTC) thermistors, were placed separately at different locations inside the battery module (including the four different corners, two midpoints of the long edges and two center points, as shown schematically in **Figure 6**) and attached with glue to the copper interconnect sheet close to the welding point at the positive terminal of the cell. This

Table 2. Physical properties and relevant parameters used in the simulation.

| Parameters	Value
Battery capacity, Q_batt [Ah]	4.8
1C current, i_1C [A]	4.8
Thermal conductivity of the battery material in radial direction, kT_r [W m^{-1} K^{-1}]	1.13
Thermal conductivity of the battery material in tangential direction, kT_tang [W m^{-1} K^{-1}]	28
Heat capacity of the battery material, Cp_batt [J kg^{-1} K^{-1}]	1340
Density of the battery material, rho_batt [kg m^{-3}]	2320
Thermal conductivity of the terminal material, kT_term [W m^{-1} K^{-1}]	400
Heat capacity of the terminal material, Cp_term [J kg^{-1} K^{-1}]	385
Density of the terminal material, rho_term [kg m^{-3}]	8960
Thermal conductivity of the coolant PAO, kT_cool [W m^{-1} K^{-1}]	0.14
Heat capacity of the coolant PAO, Cp_cool [J kg^{-1} K^{-1}]	2210
Density of the coolant PAO, rho_cool [kg m^{-3}]	820
Dynamic viscosity of the coolant PAO, mu_cool [Pa s]	8.2×10^{-3}
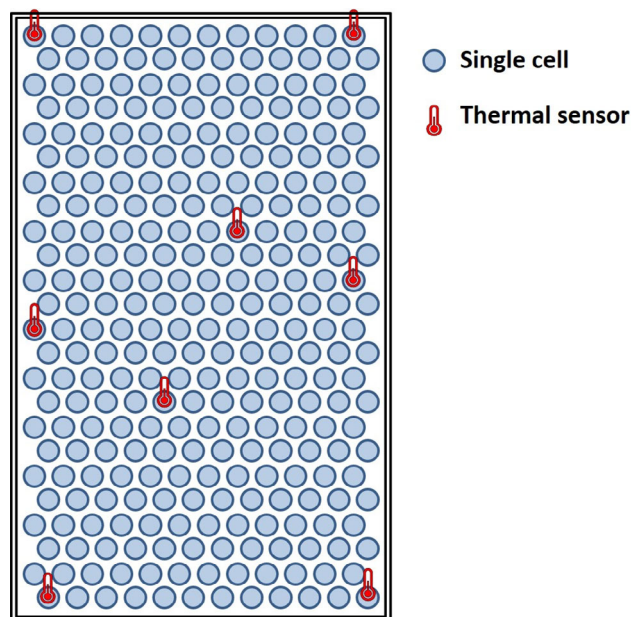
Figure 6. Schematic diagram for the module including 288 commercial 21 700 cylindrical cells, showing the locations of the eight thermal sensors used to obtain temperatures for the model validation.

provided good thermal coupling between the battery cell and the sensor. Furthermore, two temperature sensors were placed at the inlet and outlet of the coolant to measure the temperature of the liquid flow into and out of the module.

3.2. Comparison Between Experimental and Simulation Results

The integrated flow–electric-thermal model introduced in Section 2 was used to perform the simulation, and the physical

properties and relevant parameters used in the simulation are depicted in Table 2. All boundary and initial conditions were kept the same as for the validation experiment. **Figure 7**a,b shows the comparison of the temperature of the batteries and cooling liquid at the inlet/outlet between the experimental and simulation results, respectively.

The colored area in Figure 7a shows the distribution range of all the experimentally measured temperatures at different locations on the module. The simulated temperatures are shown by symbol lines, using the temperatures at the same welding points as in the experimental measurements. It can be seen that the simulated temperatures of the batteries fall within the distribution range of the measured temperatures. To demonstrate the necessity of using the 4D state-dependent parameters as input for the model, one simulation was also done assuming the internal resistance of the battery being equal to 35 mΩ (a value given by the manufacturer). This is also how many other works calculate the heat generation rate in a thermal model at the battery module/pack level.[6,20,30,31,35,38,54,55] It is clearly seen that the temperature measured experimentally fits better with the simulation results when using the state-dependent parameters. This may be due to the fact that the internal resistance given in the datasheet is most likely measured at room temperature, but the initial and inlet temperature of the coolant is set to 12 °C here. As seen in Figure 5, the internal resistance of the battery increases at a lower temperature. Thus, the temperature increase of the battery will be underestimated if a fixed internal resistance is used for a lower operational temperature. A similar comparison has also been done at relatively high temperature (32, 44 °C), but there are not very significant differences seen. This is reasonable since the measured internal resistance at higher temperatures converges to the value provided by the manufacturer. Additionally, the temperatures of the cooling liquid at the inlet and outlet of the module are also compared in Figure 7b. Except that the temperatures measured experimentally are noisier, which may be due to the nonuniformity of the thermal properties

(e.g., thermal capacity, thermal conductivity) caused by the complexity of the mechanism of the whole module, the experimental and simulated liquid temperatures compare quite well for both inlet and outlet points. This further shows that the proposed model here can relatively precisely mimic the investigated module system.

4. Model Application

Compared to experimental methods, modeling and simulation has considerably larger flexibility to investigate the effect of different parameters and thereby providing directions for the coolant selection, cooling strategy decision, module design, etc. Some of these applications will be investigated in the following.

4.1. Improved Temperature Uniformity by Using a Parallel Cooling Configuration

As mentioned in the introduction, the parallel cooling configuration (blue arrows shown in **Figure 8**a) is favorable to improve the temperature uniformity in a battery module compared to the series cooling configuration (red arrows shown in Figure 8a). To better understand the background to this phenomenon, both configurations have been simulated based on the same working conditions as the one used in the model validation, i.e., the batteries in the module were discharged from 90% to 20% with a 2C discharge current, using a PAO coolant and a flow rate of 20 mL min^{-1} per cell. Since the cooling efficiency of the series cooling configuration is strongly dependent on the number of batteries the coolant passed, and the largest temperature difference is between the first and last row of batteries, it is necessary to build a model that includes all batteries in a module to estimate this difference. Due to the extremely large computational costs for a 3D model built for a module containing 288 batteries, here a simplified 2D model which only considers the variations in the
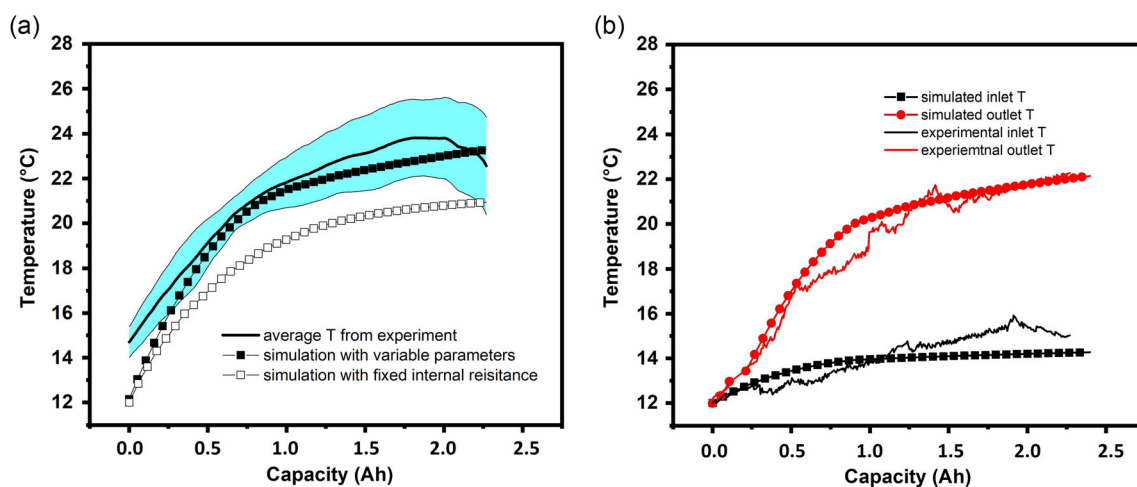

Figure 7. Temperature monitored from a battery module with direct cooling liquids as a function of the capacity during discharge from 90% SOC to 20% SOC with a 2C current. a) The solid line is the average of the battery temperature measured experimentally, with the colored area representing the distribution range of the measured data at different locations, filled symbols are simulated battery temperature using variable parameters, and open symbols are simulation results when keeping the internal resistance at a fixed value. b) Solid lines denote the experimentally measured temperatures of the liquid at the inlet (black) and outlet (red), while symbol lines are the corresponding simulation results.
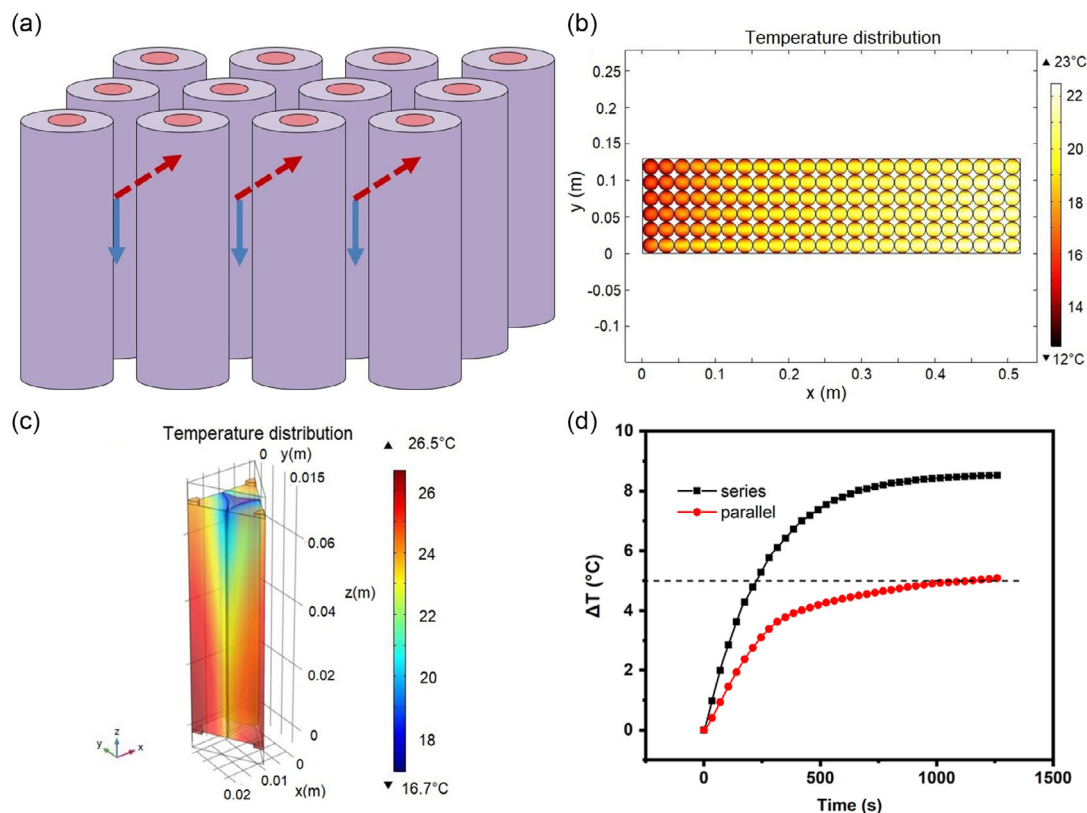
**ADVANCED
SCIENCE NEWS**
www.advancedsciencenews.com

Energy Technology
Generation, Conversion, Storage, Distribution
www.entechnol.de

Figure 8. a) Series (red) and parallel (blue) cooling configurations, b,c) simulated temperature distribution of batteries in the module by employing series (top view) and parallel cooling configuration, and d) temporal evolution of the temperature difference between the highest and lowest surface temperature of the batteries.

horizontal direction was built for comparison. Figure 8b,c shows the temperature distributions calculated based on the series cooling model and parallel cooling model, respectively. It is clearly seen that the largest temperature difference for the serial cooling configuration is found between the batteries in the first and the last row. In contrast, the largest temperature difference for parallel cooling configuration is found between the top and bottom surfaces of the same battery. This difference should then be the same for all the batteries, provided that the coolant can be distributed uniformly across the whole module.

A quantitative temporal evolution of the temperature difference calculated for series and parallel cooling configurations is shown in Figure 8d. As can be seen, the temperature difference is effectively controlled within 5 °C by using the parallel cooling configuration, while the temperature difference reaches 9 °C by using the series cooling configuration. It should be noted that the temperature difference is shown in Figure 8d is calculated using the highest surface temperature of the batteries minus the lowest surface temperature, and not using the highest/lowest temperature of the entire domain. This is due to that the core temperature of the battery is not only determined by the cooling dynamic of the coolant, but also influenced by the heat transport from the core area to the surface of the battery (within the solid phase). This will be discussed more later (Section 4.2).

Nevertheless, according to Figure 8, the parallel cooling configuration provides better cooling efficiency as compared to the series cooling configuration under the same coolant flow rate. In this context, it should be pointed out that to achieve the same flow rate in a system with typical serial cell-to-cell coolant flow, there will be an incremental pressure loss at each cell that may add up to a relatively high total pressure to drive the necessary coolant flow.[48] Thus, the energy consumption to pump coolant for such a system is extra high. Moreover, the relatively high pressure requires a more robust mechanical design of various components such as pipes, couplers, enclosures, etc. elevating design cost further, and which also implicates advantages for the cooling system with parallel configuration.

4.2. Effect of the Coolant Flow Rate

In addition to surface temperature, the cell core temperature is even more crucial to improve the energy efficiency and safety during battery usage. As one of the most important advantages of the modeling and simulation, the details of different coupled physical phenomena and dynamic changes of different variations can be analyzed straightforwardly. Information about the battery core temperature during operation is one such example.

For comparison, the same discharge process as the one used in chapter 4.1 was also used here, i.e., the battery was discharged from 90% to 20% with a 2C discharge current and using a parallel cooling configuration with the PAO coolant to control

temperature increase in the module. Results are shown in **Figure 9**, in which the black line represents calculations using the battery properties listed in Table 2. Specifically, the thermal conductivity of the solid phase of the battery material is assumed to be calculated by lumping the thermal conductivity of different layers in parallel or in series, and with different values in tangential ($k_{T,tang} = 28\ \mathrm{W\ m^{-1}\ K^{-1}}$) and radial ($k_{T,r} = 1.13\ \mathrm{W\ m^{-1}\ K^{-1}}$) directions. According to the black line in Figure 9, the core temperature of the battery, which is here referred to as the highest temperature in the core domain of the battery, as expected, increased more with a lower flow rate of the coolant. Specifically, with a flow rate of 24 mL min^{-1} per cell, the core temperature increased by 15 °C compared with the initial temperature of 12 °C. Compared to the increase in surface temperature (≈5 °C) discussed above, the effect on the core temperature increase is more dramatic.

To control the increase in temperature and to improve the efficiency of the coolant circuit, the flow rate of the coolant passing through the module can be increased. As can be seen from the black line of Figure 9, the core temperature increase is lower at a higher flow rate. Furthermore, the slope of the line decreases with increasing flow rate. This is reasonable, considering that the core temperature of the cell is influenced by two dynamic thermal processes. First, after generation from different electrochemical processes, the heat needs to be transported through the solid material to the battery surface. Second, the heat needs to be dissipated from the battery surface to the cooling liquid. The flow rate of the cooling liquid (shown in Figure 9) can directly only affect the later process, i.e., heat dissipation from the battery surface to the liquid. With a high flow rate, this heat dissipation is fairly fast. Thus, the final cooling efficiency is more limited by the heat transport within the solid material of the battery. To verify this interpretation, the thermal conductivity in the radial direction of the battery is artificially increased to 5 W m^{-1} K^{-1}, compared with the original value of 1.13 W m^{-1} K^{-1}. The simulated core temperature under different flow rates is plotted as the red line in Figure 9. It is clearly seen that the core temperature
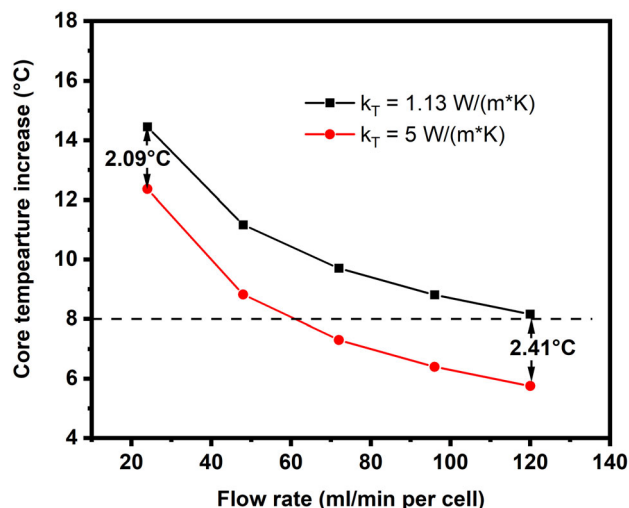
increased less (≈2–2.5 °C) with the same flow rate of the coolant if the radial thermal conductivity of the battery is increased. From the module design point of view, if the aim is to control the core temperature increase within 8 °C for a relatively low thermal conductivity (1.13 W m^{-1} K^{-1}), the flow rate of the applied coolant needs to be as high as 120 mL min^{-1} per cell. While, if the thermal conductivity of the battery can be increased (to 5 W m^{-1} K^{-1}) by some measures, for instance, an optimized battery design or improvement of the battery material's heat conduction properties, the flow rate of the coolant only needs to be 60 mL min^{-1} per cell. This is more easily achievable and can save much of the energy needed to pump coolant into the module.

4.3. Modification of Battery Module Design

Apart from increasing the flow rate, the cooling efficiency can also be improved by an appropriate modification of the module design. **Figure 10**a shows the cross-section of one battery and all its neighboring coolant units for the most commonly used battery module design in the direct liquid cooling system.[53,54,56–58] The modeling unit adopted in the simulation is shown in Figure 10a'. The module design can be modified by inserting a cylindrical rod made of an electrically and thermally insulating material (e.g., glass fiber reinforced nylon) into each of the coolant units, and keeping this cylindrical rod tangentially contacted with all three surrounding batteries. The cross-section of the modified module is shown in Figure 10b, the same as the one introduced in Section 2.1. Through this approach, the hydraulic diameter D_h is reduced according to Equation (9), where A is the cross-sectional area of the flow and P is the wetted perimeter of the cross-section.

$$D_h = \frac{4A}{P} \tag{9}$$

In fluid dynamic, the Nusselt number (Nu) is the ratio of convection to conductive heat transfer at a boundary of a fluid. It is closely related to Rayleigh number of the fluid. For a forced convection in a fully developed laminar pipe flow, the Nusselt number tends toward a constant value. For internal flow

$$Nu = \frac{h \times D_h}{k_T} \tag{10}$$

where D_h is the hydraulic diameter, k_T is the thermal conductivity of the fluid and h is the convective heat transfer coefficient. Specifically, for convection with uniform heat flux for circular tubes (which is most relevant to the model settings in this study) the Nusselt number has a value of around 4.36.[59] Considering that the thermal conductivity of the fluid is constant, a reduction in the hydraulic diameter (D_h) will lead to an increase in the convective heat transfer coefficient and thus increase the heat dissipation rate from the battery surface to the cooling liquid. As a verification, a comparison of the average battery temperature between the different module design configurations shown in Figure 10a,b as displayed in Figure 10c. It is clearly seen that for the modified module design with inserting isolators, the average temperature of the battery increases less (4 °C) as compared to the original design.

In practical module design, the isolator rod increases the total flow resistance by 20%. Assuming predominantly laminar flow
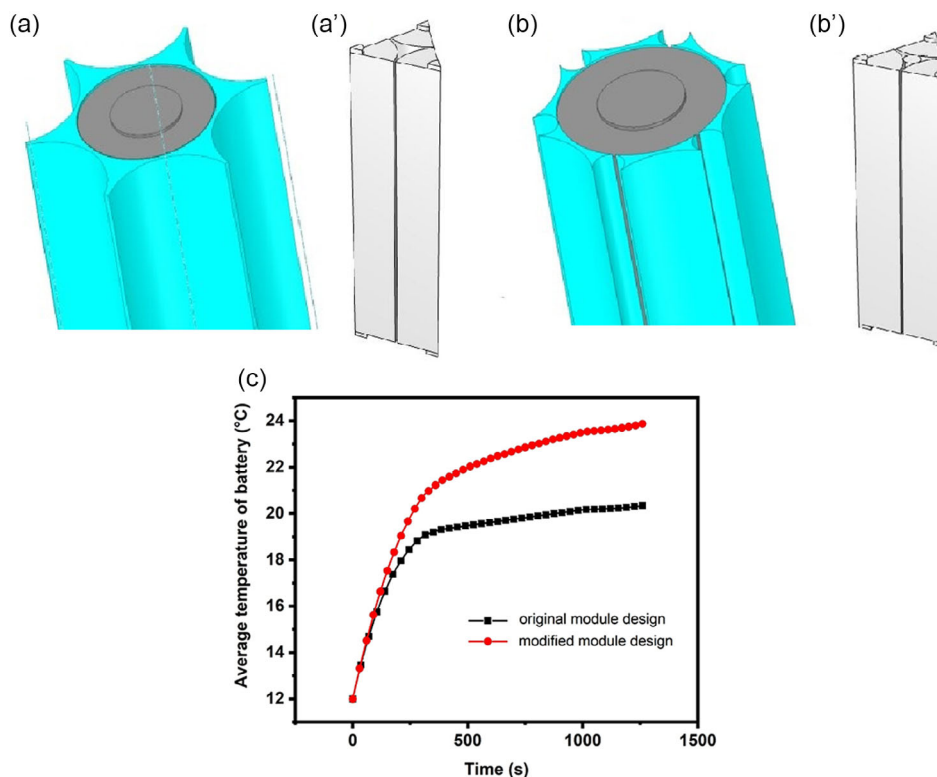

Figure 9. Simulated battery cell core temperature increase under different flow rates of the coolant. The battery is discharged with a 2C current from 90% to 20% and with polyalphaolefin(PAO) as a coolant.

Figure 10. Cross-section and model unit including one battery and all its neighboring coolant units: a) (a') for the original module design, b) (b') for the modified module design, and c) comparison of the development of average battery temperature during discharge for different module design configurations.

conditions, this also increases the pump power by 20%, but the heat transfer coefficient is increased by 100% and the liquid volume around the battery cells decreases by 50%. The total liquid volume is an important parameter to minimize in direct cooled systems, because it affects the energy density of the total battery system. In addition, from a battery module design point of view, by inserting one isolator in the volume between each of three neighboring cells and making sure that the isolator is in tangency contact with all three cells, it helps to warrant that all cells are separated effectively and uniformly. Thus, the method proposed here can effectively improve the quality of the module design both economically and technically.

5. Conclusions

This study establishes an integrated model of a LiB module by coupling first-order ECMs for the individual cells with a 3D thermal model, mimicking a representative unit for the cooling liquid used for direct liquid cooling in a parallel module design. Relevant parameters used in the ECMs, including OCP, $R0$, $R1$–$C1$ are determined through pulse-relaxation tests under different temperatures and C rates. By fitting the experimental data, a series of 4D SOC/C-rate/temperature-dependent parameters are determined and used as input for the integrated model. This makes it possible to take the transient and state-dependent battery properties into account. According to the simulations, the uniformity of the surface temperature of the batteries, which is usually the only factor that can be monitored experimentally, is better for the parallel cooling configuration compared to the series configuration. However, the increase of the core temperature cannot be efficiently controlled only by increasing the flow rate of the cooling liquid. Determination of the flow rate should balance the gain from temperature control and the energy consumed by liquid pumping. The simulation also provides directions for the modification of module design, which can largely save expensive test periods for the battery manufacturers.

Supporting Information

Supporting Information is available from the Wiley Online Library or from the author.

Conflict of Interest

The authors declare no conflict of interest.

Data Availability Statement

The data that support the findings of this study are available from the corresponding author upon reasonable request.

Keywords

[1] IEA (International Energy Agency), IEA Technology Report, https://www.iea.org/reports/electric-and-plug-in-hybrid-electric-vehicles-roadmap (accessed: October 2021).

[2] IEA (International Energy Agency), IEA Technology Report, https://www.iea.org/reports/global-ev-outlook-2019 (accessed: May 2021).

[3] J. Jaguemont, L. Boulon, Y. Dubé, *Appl. Energy* **2016**, *164*, 99.

[4] L. Bodenes, R. Naturel, H. Martinez, R. Dedryvère, M. Menetrier, L. Croguennec, J.-P. Pérès, C. Tessier, F. Fischer, *J. Power Sources* **2013**, *236*, 265.

[5] J. Jaguemont, L. Boulon, P. Venet, Y. Dubé, A. Sari, *IEEE Trans. Veh. Technol.* **2016**, *65*, 4328.

[6] H. Sun, X. Wang, B. Tossan, R. Dixon, *J. Power Sources* **2012**, *206*, 349.

[7] J. M. Reniers, G. Mulder, D. A. Howey, *J. Electrochem. Soc.* **2019**, *166*, A3189.

[8] S. Abada, G. Marlair, A. Lecocq, M. Petit, V. Sauvant-Moynot, F. Huet, *J. Power Sources* **2016**, *306*, 178.

[9] A. A. Franco, A. Rucci, D. Brandell, C. Frayret, M. Gaberscek, P. Jankowski, P. Johansson, *Chem. Rev.* **2019**, *119*, 4569.

[10] S. Tippmann, D. Walper, L. Balboa, B. Spier, W. G. Bessler, *J. Power Sources* **2014**, *252*, 305.

[11] T. Waldmann, M. Wilka, M. Kasper, M. Fleischhammer, M. Wohlfahrt-Mehrens, *J. Power Sources* **2014**, *262*, 129.

[12] F. Leng, C. M. Tan, M. Pecht, *Sci. Rep.* **2015**, *5*, 12967.

[13] T. M. Bandhauer, S. Garimella, T. F. Fuller, *J. Electrochem. Soc.* **2011**, *158*, R1.

[14] D. Lisbona, T. Snee, *Process Saf. Environ. Prot.* **2011**, *89*, 434.

[15] K. Somasundaram, E. Birgersson, A. S. Mujumdar, *J. Power Sources* **2012**, *203*, 84.

[16] M. Xu, Z. Zhang, X. Wang, L. Jia, L. Yang, *Energy* **2015**, *80*, 303.

[17] S. Panchal, M. Mathew, R. Fraser, M. Fowler, *Appl. Therm. Eng.* **2018**, *135*, 123.

[18] H. Liu, Z. Wei, W. He, J. Zhao, *Energy Convers. Manage.* **2017**, *150*, 304.

[19] L. Yin, A. Björneklett, E. Söderlund, D. Brandell, *J. Energy Storage* **2021**, *39*, 102648.

[20] X. Lin, H. E. Perez, S. Mohan, J. B. Siegel, A. G. Stefanopoulou, Y. Ding, M. P. Castanier, *J. Power Sources* **2014**, *257*, 1.

[21] Y. Ye, Y. Shi, N. Cai, J. Lee, X. He, *J. Power Sources* **2012**, *199*, 227.

[22] W. B. Gu, C. Y. Wang, *J. Electrochem. Soc.* **2000**, *147*, 2910.

[23] B. Wu, V. Yufit, M. Marinescu, G. J. Offer, R. F. Martinez-Botas, N. P. Brandon, *J. Power Sources* **2013**, *243*, 544.

[24] P. Peng, F. Jiang, *Int. J. Heat Mass Transf.* **2016**, *103*, 1008.

[25] G. Guo, B. Long, B. Cheng, S. Zhou, P. Xu, B. Cao, *J. Power Sources* **2010**, *195*, 2393.

[26] Y. Tang, L. Wu, W. Wei, D. Wen, Q. Guo, W. Liang, L. Xiao, *Appl. Therm. Eng.* **2018**, *137*, 11.

[27] U. S. Kim, C. B. Shin, C.-S. Kim, *J. Power Sources* **2008**, *180*, 909.

[28] K.-J. Lee, K. Smith, A. Pesaran, G.-H. Kim, *J. Power Sources* **2013**, *241*, 20.

[29] T. Yamanaka, Y. Takagishi, T. Yamaue, *J. Electrochem. Soc.* **2021**, *168*, 050545.

[30] N. Wang, C. Li, W. Li, M. Huang, D. Qi, *Appl. Therm. Eng.* **2021**, *192*, 116932.

[31] J. Zhang, X. Wu, K. Chen, D. Zhou, M. Song, *J. Power Sources* **2021**, *490*, 229539.

[32] D. Bernardi, E. Pawlikowski, J. Newman, *J. Electrochem. Soc.* **1985**, *132*, 5.

[33] K. Chen, M. Song, W. Wei, S. Wang, *Energy* **2018**, *145*, 603.

[34] Z. Liu, J. Huang, G. Jiang, Q. Yan, J. Hu, *Appl. Therm. Eng.* **2021**, *185*, 116415.

[35] T. Ahmad, A. Mishra, S. Ghosh, C. S. Casari, *Energy Technol.* **2021**, *10*, 2100888.

[36] Y. Ding, M. Wei, R. Liu, *Appl. Therm. Eng.* **2021**, *186*, 116494.

[37] W. Wu, X. Xiao, X. Huang, *Electrochim. Acta* **2012**, *83*, 227.

[38] Y. Fan, Y. Bao, C. Ling, Y. Chu, X. Tan, S. Yang, *Appl. Therm. Eng.* **2019**, *155*, 96.

[39] H. Zhou, F. Zhou, L. Xu, J. Kong, Q. Yang, *Int. J. Heat Mass Transf.* **2019**, *131*, 984.

[40] N. Yang, X. Zhang, G. Li, D. Hua, *Appl. Therm. Eng.* **2015**, *80*, 55.

[41] P. Nelson, D. Dees, K. Amine, G. Henriksen, *J. Power Sources* **2002**, *110*, 349.

[42] A. Samba, *Doctor Thesis*, Vrije Universiteit Brussel (Belgique), **2015**.

[43] W. Yang, F. Zhou, H. Zhou, Q. Wang, J. Kong, *Appl. Therm. Eng.* **2020**, *175*, 115331.

[44] W. A. Hermann (Tesla Motors Inc.), US8263250B2, **2012**.

[45] G. Bower, Chevy Bolt 200 Mile EV Battery Cooling and Gearbox Details, https://insideevs.com/chevy-bolt-200-mile-ev-battery-cooling-and-gearbox-details-bower/ (accessed: January 2016).

[46] Rimac-automobili, Rimac Helps Bring World's Most Powerful Production Car to Reality, http://www.rimac-automobili.com/en/press/releases/rimac-helps-bring-world-s-most-powerful-production-car-to-reality/ (accessed: May 2015).

[47] F. Lambert, Aston Martin's Upcoming New Hypercar will have a Battery Pack Supplied by Rimac, https://electrek.co/2017/02/16/aston-martin-hypercar-electric-battery-pack-rimac/ (accessed: February 2017).

[48] G. Xia, L. Cao, G. Bi, *J. Power Sources* **2017**, *367*, 90.

[49] C. J. Seeton, *Tribol. Lett.* **2006**, *22*, 67.

[50] D. F. Rogers, *Larminar Flow Analysis*, Cambridge University Press, New York, NY **1992**.

[51] S. S. Madani, E. Schaltz, S. K. Kær, *Batteries* **2018**, *4*, 20.

[52] R. Jackey, J. Gazzarri, Automating battery model parameter estimation using experimental data, https://www.mathworks.com/videos/automating-battery-model-parameter-estimation-using-experimental-data-81987.html (accessed: August 2013).

[53] C. Roe, X. Feng, G. White, R. Li, H. Wang, X. Rui, C. Li, F. Zhang, V. Null, M. Parkes, Y. Patel, Y. Wang, H. Wang, M. Ouyang, G. Offer, B. Wu, *J. Power Sources* **2022**, *525*, 231094.

[54] S. Park, D. Jung, *J. Power Sources* **2013**, *227*, 191.

[55] M. Tousi, A. Sarchami, M. Kiani, M. Najafi, E. Houshfar, *J. Energy Storage* **2021**, *41*, 102910.

[56] X. Tan, P. Lyu, Y. Fan, J. Rao, K. Ouyang, *Appl. Therm. Eng.* **2021**, *196*, 117279.

[57] S. Wu, L. Lao, L. Wu, L. Liu, C. Lin, Q. Zhang, *Appl. Therm. Eng.* **2022**, *201*, 117788.

[58] B. Ruhani, A. Abidi, A. K. Hussein, O. Younis, M. Degani, M. Sharifpur, *J. Energy Storage* **2022**, *45*, 103714.

[59] F. P. Incropera, D. P. DeWitt, *Fundamentals of Heat and Mass Transfer*, 2nd ed., Wiley, Hoboken, NJ **2001**.